Science and Technology Indonesia
e-ISSN:2580-4391 *p*-ISSN:2580-4405
Vol. 7, No. 3, July 2022

Research Paper

Study of the Electrical, Optical and Morphological Properties in Submicron and Microstructured ZnO Thin Films Obtained by Spin Coating and Chemical Bath Deposition

C. López-Esmerio[1], C. Ruiz-Rojas[2], J. Angulo-Rocha[3], E. Lizárraga-Medina[4], F. Ramos-Brito[5]*, E. Camarillo-García[6], R. Martinez-Martinez[7], M. Aguilar-Frutis[8], M. García-Hipólito[9]

[1]*Master student at Posgrado en Ciencias Físicas, Instituto de Física, Universidad Nacional Autónoma de México, Ciudad de México, 01000, México*
[2]*PhD student at Posgrado en Tecnología Avanzada at CICATA-Legaria, Instituto Politécnico Nacional, Ciudad de México, 11500, México*
[3]*Hospital de la Mujer, Secretaría de Salud Sinaloa, Culiacán, 80020, México*
[4]*Master student at Posgrado en Tecnología Avanzada at CICATA-Legaria, Instituto Politécnico Nacional, Ciudad de México, 11500, México*
[5]*Laboratorio de Síntesis de Materiales, Facultad de Ciencias Físico Matemáticas, Universidad Autónoma de Sinaloa, Ciudad Universitaria, Culiacán, 80000, México*
[6]*Instituto de Física, Universidad Nacional Autónoma de México, Ciudad de México, 01000, México*
[7]*Universidad Tecnológica de la Mixteca, Oaxaca, 69000, México*
[8]*CICATA-Legaria, Instituto Politécnico Nacional, Ciudad de México, 11500, México*
[9]*Instituto de Investigaciones en Materiales, Universidad Nacional Autónoma de México, Ciudad de México, 04150, México*
***Corresponding author**: framosbrito@uas.edu.mx, ramosbritof@gmail.com

Abstract
In the present work the synthesis of ZnO semiconductor thin films was performed successively using spin coating and chemical bath deposition techniques. The deposition was made by varying the concentration of zinc acetate and hexamethylenetetramine (HMTA: ZnAc) in the precursor solution. This process led to two preferred growth directions (002) and (101), both with very similar texture coefficients, too; a noticeable change in morphology of structured surface, variation in unit cell parameters and crystalline grain size. All the films turned out homogeneously submicro and microstructured and with a wurtzite-type hexagonal crystalline structure. Using pre-loaded Mathematica 11.3 software functions and an algorithm developed in it, the micrographies were analyzed to calculate the percentage of substrate-covered area which was always greater than 80%. Likewise, it also found that resistivity decreases at a higher percentage of covered area and that the variation in the shape of the photo luminescent emission spectrum can be considered as a qualitative indication of the concentration of charge carriers.

Keywords
ZnO Semiconductor, Nanostructured Films, Texturized Films, n-Type Semiconductor

Received: 19 February 2022, Accepted: 31 May 2022
https://doi.org/10.26554/sti.2022.7.3.291-302

1. INTRODUCTION

Over the past decade, semiconductor research has grown considerably. This is due to the potential applications they may have, as well as the fact that nowadays we have better infrastructure at hand, such as better labs and supercomputers. The field of application of semiconductor materials is very wide and varied, they are present in products as common as sunscreen but also in the most sophisticated electronic devices, without exception of those that are now considered essential by most human beings to carry out their daily lives, such as: smartphones, televisions, tablets, and computers, which are now the trend for the semiconductor industry (Yeap, 2013). Likewise, they also made a difference in the lucratively growing area of lighting devices, this, since the introduction of LED in the 60's and its constant improvement since then (Gayral, 2017; Weisbuch, 2018). There are other areas where the introduction of semiconductor materials has played an important role for their development, such as: food, health, energy, and environment (Weisbuch, 2018; Nanda et al., 2017; Karthikeyan et al., 2020; Zhu and Zhou, 2019); a clear example for this is the use of semiconductors in the production of solar cells that can convert solar energy into electricity, or the treatment of sewage waters through photocatalysis using semiconductor materials.

The formerly-mentioned great success of semiconductors is due to the large amount of knowledge generated on them as a result of the investigations carried out on their different properties: morphological, optical, electrical, chemical, etc., only in this nearly-concluding decade, it has been reported, according to the Central Library's online database from Universidad Nacional Autónoma de México (bc.unam.mx), 977 591

scientific publications that mention the word semiconductor and are estimated to be around 2,076,660 for the next decade. The notable development reported by the different areas when they incorporate semiconductors in its processes has led to hard work in the semiconductor research from different areas: both experimental, numerical calculations with supercomputers and theory, all in the same direction, getting better semiconductors with certain properties that help to solve different needs.

Zinc oxide is one of the semiconductors that have recently caught the attention of multiple research groups, in the first decade of this century, according to the database of the bc.unam.mx, 413 scientific publications were reported for "zinc oxide semiconductor" and in this near-to-end decade, it has been reported in the order of 1420, estimating the order of 5500 publications for the next decade.

ZnO is considered an attractive and potentially promising semiconductor for a wide variety of applications, this is because it has an energy gap of 3.37 eV, exciton link energy 60 meV to 300°K (Özgür et al., 2005a), in addition to being transparent in the visible region of the wavelength spectrum.

Among the possible applications for ZnO there are: ultraviolet (UV) lasers (ZKTang et al., 1998), light emitting diodes (LED) (Park et al., 2010), PN junction devices (Bian et al., 2004), transparent thin film transistors (Carcia et al., 2006), gas sensors (Chou et al., 2006), and dental cements considering that its biosecurity has been proven (Nguyen et al., 2019). Furthermore, 10 years ago it was revealed that ZnO nanoparticles have the potential to selectively kill tumor cells, performing studies with different tumor entities (Hanley et al., 2008; Vandebriel and De Jong, 2012; Pandurangan et al., 2016; Wahab et al., 2016; Chandrasekaran and Pandurangan, 2016; Gupta et al., 2015; Kc et al., 2016; Hassan et al., 2017), although the exact mechanism of Cytotoxicity is still subject to debate (Vandebriel and De Jong, 2012).

Various synthesis techniques have been used to grow ZnO films (Lu et al., 2007; Kim et al., 2000; Lu et al., 2000; Zhang et al., 2010; Shinde et al., 2010; Muiva et al., 2011) but it is important to highlight those that offer simplicity, high growth rate, homogeneity and production at a low cost. Among these, some of the most common are Spin Coating and Chemical Bath Deposition. There are works that report the growth of micro and nano ZnO bars on buffers deposited by Spin Coating using Chemical Bath Deposition (Chen and Ting, 2016; Wu et al., 2010; Rana et al., 2017; Suhaimi and Yuwono, 2019; Chang et al., 2017), that is, using a process that involves these two techniques. The virtue of employing this process is that it allows growing micro/nano ZnO bars aligned and oriented (Chang et al., 2017). The buffer layer deposition provides nucleation centers that reduce interface energy between the substrate and the reagents and allows the vertically aligned bars to form at the substrate surface due to heterogeneous nucleation. The morphology, the degree of alignment, the density, crystalline quality and optical properties of micro and nano bars are directly related to the parameters of the buffer (Chang et al., 2017). Likewise, the study on the effect that this buffer has on the properties of the micro and nano bars has concluded that the diameter of these increases linearly with the crystalline grain size of the buffer (Chang et al., 2017), that the length of these is proportional to the time in the chemical bath as $t^{1}.5$ and that the area density decreases with the roughness of the buffer layer (Chen and Ting, 2016).

There are very significant advances in potential applications for ZnO, specifically in those that imply that it has an optimal semiconductor property, two examples of this are: 1) as a transparent conductive oxide, there are works where the properties of commercial ITO, and ZnO thin films doped with indium (I) gallium (Ga) and aluminum (Al) are compared, having very similar resistivities, of the order of 10^{-4} Ω.cm, with ZnO presenting higher mobility (Gonçalves et al., 2011) and 2) in LED's (Rahman, 2019), ZnO is presented as the naturally most viable semiconductor to replace GaN in diode manufacturing for short wavelength light emitters due to the ZnO energy gap and its exciton link energy that it is more than twice that of GaN; however, much remains to be done. The research reported in this direction shows that a way to deal with the vicissitudes that have been presented, is through systematic studies on the synthesis of ZnO as a function of the different synthesis parameters, this through synthesis processes that allow: reproduce the ZnO obtained, such as Spin Coating and Chemical Bath Deposition, as well as induce changes in its electrical properties based on its other properties such as: morphology, crystal structure, texture and optical properties, among others. This in order to study the former as a function of the latter and fully understand the different processes that give it its semiconductor property and the correlation between them. Surely this will allow, in the future, to develop a synthesis process that is attractive and scalable at the industrial level to manufacture ZnO in line with specific semiconductor characteristics that allow its incorporation in the market and the partial or total displacement of the material to replace.

This work presents an investigation that deals with the synthesis and systematic characterization of ZnO micro / nano structured semiconductor films by deposition by Chemical Bath Deposition on glass substrates previously coated with a layer ZnO buffer by Spin Coating. For this work, a systematic synthesis of microstructured ZnO was achieved through a process employing spin coating for the deposition of a buffer layer over glass substrates, followed by Chemical Bath Deposition to grow a microstructured thin film of ZnO over the buffer. The objective for this investigation work is to obtain films with varying morphology and texture, in addition to seeing how those variations can affect optical and electrical properties for ZnO. Among the results obtained there is the fact that: the synthesis process used favors two preferred texture directions, (002) and (101) depending on the synthesis conditions and without noticeable changes between the coefficients of texture both for address (002) and address (101); the concentration of charge carriers was found to be higher for the textured films in the address (101) than for those in address (002); the higher the percentage of substrate-covered area, the lower the resistiv-

ity, regardless of the morphology and texture; the difference between photoluminescent emissions associated with donor defects (Zn_i0 y Zn_i) and V_{Zn} acceptors can be considered as a parameter indicative of the charge carrier concentration; the greater the difference, the greatest the concentration of n-type charge carriers. These results encourage the use of high resolution photoluminescence spectroscopy to quantitatively measure the difference between type "n" and "p" charge carriers in ZnO. This could place photoluminescence spectroscopy as an optical method for characterizations that until this day are done only via electrical techniques.

2. EXPERIMENTAL DETAILS

2.1 Synthesis

Thin films of ZnO were synthesized on glass substrates, the techniques used in the synthesis were spin coating and chemical bath deposition, by means of the first one the film that served as a buffer layer to later grow the second one on it. For buffer films the precursor solution was prepared with zinc acetate dehydrate ($(CH_3COO)_2Zn.2H_2O$) from the brand J.T. Baker USA and methanol with a purity of 99.8% as solvent, with a concentration of 0.06 M (200 mL of methanol and 2.63 g of zinc acetate). The spin coating process was done with a KW-4A spin-coater model from Chemat Technology, the equipment was configured with two turning stages, the first at 800 RPM for 9 s and the second at 2500 RPM for 30 s. For each buffer film, was used a droplet of 100 μL, then, after spinning the glass was placed on an IKA brand grill HS-7 model for 10 minutes at 80°C.

The synthesis of ZnO thin films was achieved by Chemical Bath Deposition, using the same zinc precursor as above mentioned and adding deionized water with a resistivity of 18 MΩ as solvent, in addition, an organic compound that acts as a complexing agent was added, hexamethylenetetramine ($(CH_2)_6N_4$). For the precursor solution, the zinc acetate solution was dissolved in deionized water at 0.024 M, this solution was divided into 7 beakers to which hexamethylenetetramine (HMTA) was added. To achieve homogeneity in the solution this was placed for 5 minutes in an ultrasonic bath in a from the brand Branson, model 1800. The samples were then placed in the chemical bath at a temperature of 78°C for 12 hours. The parameter that was varied was the relative concentration between zinc acetate and HMTA (HMTA: ZnAc) in the precursor solution, the ratios were: 0.0625: 1, 0.125: 1, 0.1875: 1, 0.3125: 1, 0.375: 1, 0.54: 1, and 0.625: 1, which from here on will be named C1, C2, C3, C4, C5, C6, and C7, respectively.

2.2 Characterization

The diffraction patterns of all ZnO films, Figure 1, were obtained with a diffractometer from the brand BRUKE model D8 ADVANCE. The crystallite size (D) strain (ε), stress (σ) and energy density (u) values were calculated by using Scherrer formula and the modified Williamson-Hall method (W-H) (Kalita and Kalita, 2015), the results are shown in Table 1. The texture coefficient was obtained at from the intensities of (100), (002), and (101) peaks and considering the following equation (Wang et al., 2015):

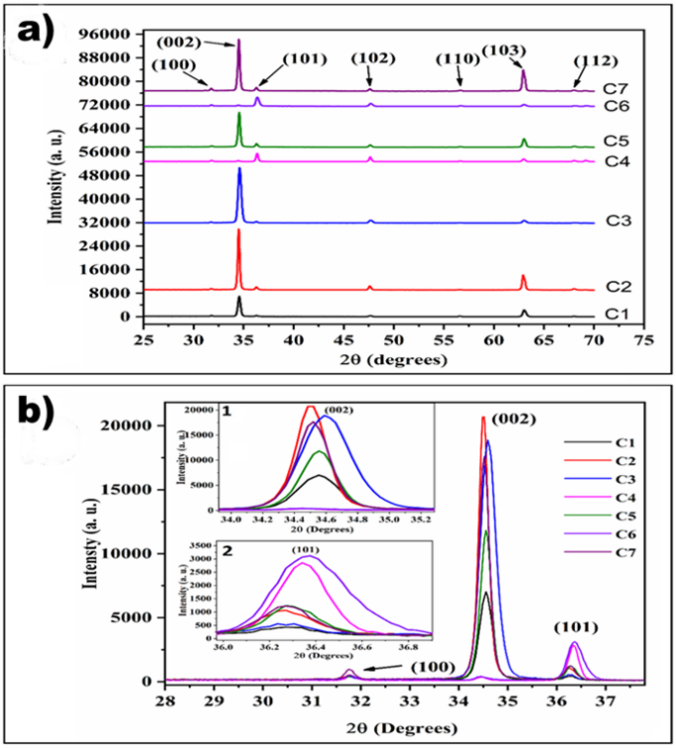

Figure 1. a) Results of X-Ray Diffraction (XRD) Analysis for All Samples Showing Their Miller Indexes Corresponding to Wurtzite Type Crystalline Structure; b) Enlarged XRD Pattern for The Zone of The (100), (002), and (101) Planes, The Inserts are an Enlargement of The Diffraction Peaks Corresponding to The Planes (002) and (101) that Show The Variation of The Unit-Cell Dimensions

$$TC_{hkl} = \frac{I_{hkl}}{I_{0hkl}} \left\{ \frac{1}{N} \sum_{N} \frac{I_{hkl}}{I_{0hkl}} \right\}^{-1} \quad (1)$$

where $TC_{(hkl)}$ is the texture coefficient of the planes hkl, $I_{(hkl)}$ is the measured intensity of the peak, $I_{0\,(hkl)}$ is the intensity of the planes hkl in a sample that shows no growth or preferential orientation and N is the number of diffractions considered in the analysis. The micrographs of the samples were obtained using the Atomic Force and Scanning Electron Microscopies (AFM and SEM), using the Thermo Microscopes Veeco model Autoprobe CP and JEOL microscope model JSM-6390LV, respectively. The electrical properties of the ZnO films were obtained with a kit from the brand ECOPIA, model HMS-3000 that measures Hall voltage. Photoluminescence spectra of the samples was obtained with an Edinburg FLS980 spectrometer. The excitation wavelength of choice was 325 nm, corresponding to a local maximum for the excitation spectrum of sample C7, which resulted to appear in all samples. The

Table 1. D, ε, σ and u Values for All Samples Extracted from Plots in Figure 2 That Correspond to Scherrer and W-H Analysis of XRD Patterns of The Samples

Sample	Scherrer method		W-H method								
	(100), (002), (101) peaks	All peaks	UDM		USDM			UDEDM			
	D (nm)		D (nm)	ε 10^{-3}	D (nm)	ε 10^{-3}	σ (Mpa)	D (nm)	ε 10^{-3}	σ (Mpa)	u (Kjm^{-3})
C1	29.73	112.72	59.74	1.15	59.11	1.06	133.25	60.85	1.11	139.43	77.51
C2	34.25	126.05	63.87	1.10	61.10	0.96	120.50	63.79	1.03	129.44	66.80
C3	27.73	254.31	66.96	1.63	62.15	1.45	182.54	65.82	1.55	193.84	149.80
C4	33.85	93.68	54.35	0.76	54.24	0.67	84.39	55.48	0.72	89.83	32.17
C5	32.20	114.59	56.80	1.02	54.03	0.86	107.39	56.57	0.93	117.40	54.95
C6	28.09	171.70	53.31	1.35	53.24	1.26	157.50	54.65	1.31	163.83	107.28
C7	34.31	117.50	60.00	0.91	57.47	0.77	96.69	59.84	0.84	105.20	44.13

transmittance of the samples was obtained using the UV-VIS-NIR Cary 5000 spectrophotometer. The percentage of the covered area of the substrate was calculated using the procedure shown in the electronic supplementary material, which includes preloaded functions of Mathemática 11.3 and an algorithm developed in it. The dimensions of the individual elements that made up the microstructure of the films were obtained by analyzing the SEM images using the "imageJ" software (Rasband, 2012).

3. RESULTS AND DISCUSSION

3.1 Crystalline Structure

Figure 1a shows the diffractograms of all samples, all of them present the peaks corresponding to the planes (100), (002), (101), (102), (110), (103), and (112) corresponding to the wurtzite type crystalline structure of ZnO. The figure shows that, except samples C4 and C6 that presented a preferential growth of the planes (101) and texturization of the surface in <101> direction, all the others presented a preferential growth of the planes (002) and texturization of the surface in direction <001>. The texture coefficients in the direction <001> for samples C1, C2, C3, C5, and C7 were: 2.7947, 2.8696, 2.9338, 2.7768, and 2.7794, respectively; while texture coefficients in direction <101> for samples C4 and C6 were 1.7857 and 1.9303, respectively.

Figure 1b presents the diffractograms for all samples, for a 2θ interval of (28.0, 37.8)°, which corresponds to the region of diffraction peaks associated with crystalline planes (100), (002) and (101) of ZnO. With the intention of pointing out the existing differences between all diffraction peaks of a same crystallographic plane for each sampes, an enlargement of respective zones was made for the diffractogram; these enlargements can be found in the inserts of Figure 1b. Insert 1 shows a small shift of the (002) peak towards the right in comparison to the position of that same peak for sample C2, this indicates a difference between interplanar distances for the samples with a prefered growth in the <001> direction, being C2 and C3 the highest and lowest values, respectively. Insert 2 shows that the peaks corresponding to planes (101) are all centered arround the same value, which would mean that the interplanar spacing did not vary for samples with a preferential growth in the <101> direction.

Taking the Bragg angle values of diffraction peaks, the interplanar distances "d" of that planes were calculated through the equation known as the Bragg's law (Cullity and Stock, 2001):

$$n\lambda = 2d\sin\theta \tag{2}$$

Where n is the order of diffraction, λ the wavelength of the x-rays and θ the diffraction peak in question.

Once the interplanar distances were calculated, the unit-cell parameters were calculated, this by means of the equation that relates "d", the Miller indices of the planes (hkl) and the "a" and "c" unit-cell parameters for a hexagonal structure (Cullity and Stock, 2001):

$$\frac{1}{d^2} = \frac{4}{3}\frac{(h^2 + hk + k^2)}{a^2} + \frac{l^2}{c^2} \tag{3}$$

The volume V of the unit-cell was obtained knowing that $V = 0.866a^2c$ (Wang et al., 2015). Table 2 shows the results obtained from V, a, c for all samples. The cell volume reached vary from 47.4344 to 47.6035 $Å^3$ and the unit cell parameter "c" from 5.1886 to 5.1999 Å.

The corresponding W-H plots (Figure 2) showed that broadening of the diffraction peaks was essentially isotropic. This indicates that diffracting domains were isotropic and there was also a microstrain contribution. Table 1 shows D, ε, σ, and u values for all samples. There are two columns for D value by Scherrer equation, for the first column was considering only (100), (002) and (101) diffraction peaks and for the second one all diffraction peaks were considered. There is a remarkable difference between values of D obtained in these two different ways, which drives to consider the lattice strain factor for

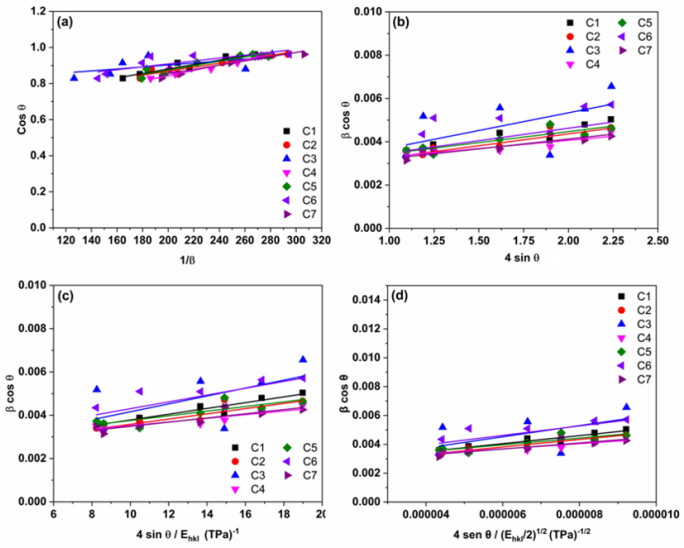

Figure 2. . Estimation of Crystallite Size (D), Lattice Strain (Σ), Stress (σ) and Energy Density (u) by Scherrer and W-H Methods. (a) Scherrer Method to Calculate D of All Samples Considering All Peaks in Their Corresponding Diffractions Patterns. Plot of cos θ vs $1/\beta$. (b) Uniform Deformation Model of W-H Method. (c) Uniform Stress Deformation Model of W-H Method. (d) Uniform Deformation Energy Density Model of W-H

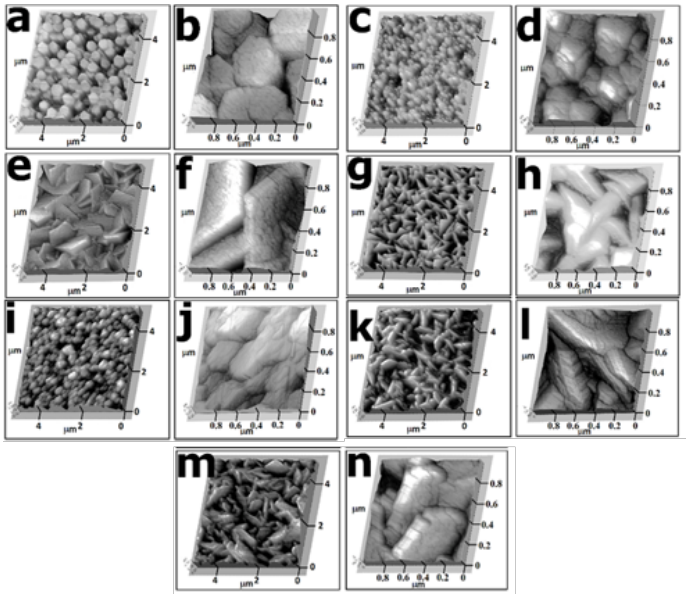

Figure 3. Atomic Force Microscopy Results for All Samples. Each Sample was Analyzed at Two Different Resolutions in Order to Show Microstructure Details. a, b) Sample C1; c, d) Sample C2; e, f) Sample C3; g, h) Sample C4; i, j) Sample C5; k, l) Sample C6; and m, n) Sample C7

Table 2. Results Obtained from a, c and V for All The Samples

Sample	a (Å)	c (Å)	V (Å^3) = 0.866 a^{2}c
0.0625:1 (C1)	3.2528	5.1905	47.5600
0.1250:1 (C2)	3.2513	5.1999	47.6022
0.1875:1 (C3)	3.2510	5.1886	47.4900
0.3125:1 (C4)	3.2497	5.1999	47.5554
0.3750:1 (C5)	3.2500	5.1943	47.5129
0.5400:1 (C6)	3.2468	5.1958	47.4331
0.6250:1 (C7)	3.2507	5.1999	47.5846

D calculation. Table 1 shows the values of D obtained from UDM, USDM, and UDEDM, which are approximately similar, indicating that the inclusion of strain in various forms of W-H method has a very small effect on the average crystallite size of sub-microstructured ZnO films. The crystallite size resulted from W-H method was in a size of around 58.73 nm, which is in agreement with microstructure results obtained by AFM for all samples, for example: AFM images in Figures 3b and 3f show the microstructure of samples C1 and C3, respectively. However, the difference between D values obtained from the Scherrer formula and W-H methods is large, showing that is essential to estimate D by considering both crystallite size and lattice strain contributions in the widening of the diffraction peaks. This large difference was associated with the great contribution of heterogeneous microstrains in the widening of the diffraction peaks (Zhang et al., 2020). These microstrains are due to dislocations in grain boundaries regions (Zhang et al., 2020). Zhang et al. (2020) conclude in their work that assuming grain boundary structures in nanocrystalline and coarse grain materials are very similar, then the dislocation density in the grain boundary (GB) regions is almost like a material constant depending mostly on the misorientation and structure of GBs. They proposed a model that shows, on one hand, that when the grain size is smaller than about 20 nm and the grain interior regions become more-or-less free from dislocations the average dislocation density in the crystal can still be substantially large. At these small grain size values, the volume fraction of GBs becomes significant and the dislocation density in GBs becomes dominant in the entire crystal. On the other hand, even in coarse grain polycrystals, the GB regions do consist of substantial dislocation densities. Other authors whose research is about nanoparticles (Bindu and Thomas, 2014; Solati and Dorranian, 2017) and nanofilms (Yamada et al., 2007), they have reported only small differences between results obtained from Scherrer formula and W-H method attributing this to the difference in averaging the particle size distribution (Bindu and Thomas, 2014; Solati and Dorranian, 2017; Yamada et al., 2007).

Figure 4 presents the "c" parameter and volume of the unit-cell plotted as a function of the relative concentration of HMTA in the precursor solution. It is appreciated that apparently there

is no correlation between these physical characteristics of the sample and the HMTA concentration.

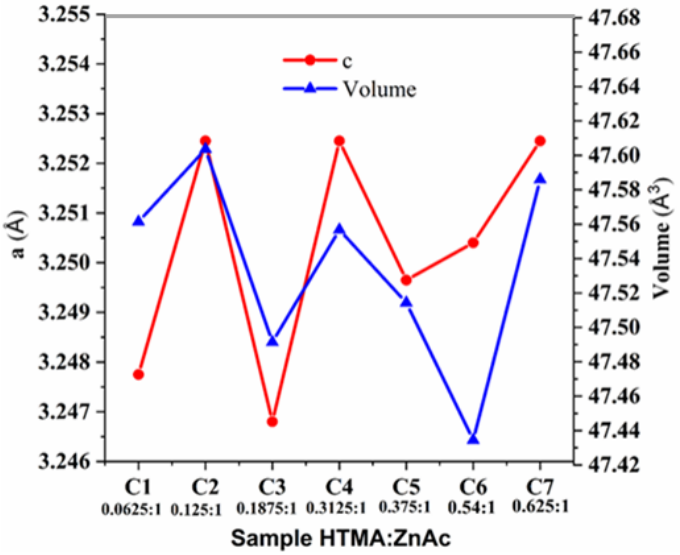

Figure 4. Parameters and Volume of The Unit-Cell Plotted as a Function of The Relative Concentration of HMTA in The Precursor Solution

3.2 Microstructure

Figures 3 and 5 show the AFM and SEM micrographs of all the samples, respectively. The congruence between the images obtained for each of the samples by both techniques, AFM, and SEM, denote the good quality of the deposit in terms of homogeneity along the entire surface of the substrate. All samples resulted in microstructured films. The C1, C2, C3, C4, and C5 films were made up entirely of ZnO bars that were moderately oriented perpendicular to the substrate and with apparently hexagonal cross section, while films C6 and C7 were made up of corn flake-like structures oriented almost perpendicular to the substrate plane.

At first glance it can be seen that the samples C1, C2 y C4 show empty spaces between the bars, that is to say, spaces where the deposition of ZnO has relatively poor, the Table 3 presents the results obtained for the percentage of substrate-covered area, in addition to: the diameter average of the cross section of the bars for samples C1, C2, and C5, the edge of the hexagonal cross section for sample C4, the thickness of the sheets in the samples C6 and C7 and the texture coefficient. The results for the diameter show a difference of up to an order of magnitude between the thinnest bars of the C2 sample and the thickest of the C3 sample. All ZnO bars show a nodular type growth and nanostructured hexagonal cross section with an average roughness of the order of crystallite grain size, i.e. for sample C1 the average roughness obtained by AFM was 24.9 nm that is consistent with its grain crystalline size of 26,975 nm calculated by Scherrer formula for the planes (002), as was shown in Table 1, which seems to indicate that the

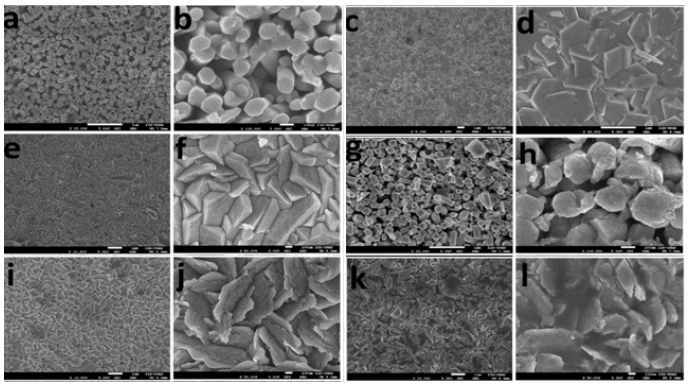

Figure 5. Scanning Electron Microscopy Results for All Samples. Each Sample was Analyzed at Two Different Resolutions in Order Two Show Microstructure Details. a, b) Sample C2; c, d) Sample C3; e, f) Sample C4; g, h) Sample C5; i, j) Sample C6; and k, l) Sample C7

nanostructures of the hexagonal upper face are single crystals of ZnO.

Table 3 shows the values of roughness considering an area of 10×10 μm^2. These values turned out to be: 63.1, 33.0, 50.0, 46.4, 47.8, 66.2, and 35.4 nm, for samples C1, C2, C3, ..., C7, respectively. All the samples presented Gauss-type histograms for the distribution of the measured heights, practically symmetrical, with no apparent bias, except for sample C1, which showed little bias pronounced towards heights of lesser value. This reaffirms what has been said about the degree of homogeneity of the coatings.

3.3 Electrical Properties

Figure 6 shows the results obtained for resistivity (Ω·cm), charge carrier concentration ($1/cm^3$) and mobility ($cm^2/V{\cdot}s$) of all samples. It is observed that samples that resulted with higher resistivity and practically in the same order of 60 Ω·cm were C1 and C2, while the rest presented lower resistivities in up to one order of magnitude, as is the case of C3, which turned out to be the one with the lowest resistivity with 4.02 Ω·cm. Likewise, samples C1 and C2 also had the fewest charge carrier concentration with values of 1.68 and 1.19×10^{17} $1/cm^3$, respectively, while samples C4 and C6 textured in address <101> resulted in the highest number of charge carriers with values of 6.84 and 6.31×10^{18} $1/cm^3$, but with the lowest mobility with values of 0.34 and 0.29 $cm^2/V{\cdot}s$, respectively. Sample C1, which, as already mentioned, turned out to be the sample with greater mobility of 3.08 $cm^2/V{\cdot}s$, up to an order of magnitude greater than those of C4 and C6, however; with a very low number of charge carriers.

Figure 6 shows that the number of charge carriers for samples C1, C2, and C5 is smaller than that for sample C3, while for samples C4, C6, and C7 it is bigger. Additionally, carrier mobility values for samples C1, C2, and C5 are much higher than for sample C3, but lower for samples C4, C6, and C7. This is not in agreement to the results presented for microstruc-

Table 3. Results Obtained for The Percentage of Substrate-Covered Area, The Diameter Average of The Bars, The Thickness of The Sheets of The Samples, and The Texture Coefficient from All Samples

Sample	Substrate-covered area (%)	Diameter average (nm)	Edge of the hexagonal cross section	Thickness of the sheets	Texture coefficient	
					<001>	<101>
0.0625:1 (C1)	94.72	338	—	—	2.7947	0.0789
0.1250:1 (C2)	81.52	126	—	—	2.8696	0.0745
0.1875:1 (C3)	99.61	1268	—	—	2.9338	0.0300
0.3125:1 (C4)	98.46	—	402	—	0.6374	1.7857
0.3750:1 (C5)	85.33	186	—	—	2.7768	0.1353
0.5400:1 (C6)	99.85	—	—	25	0.5820	1.9303
0.6250:1 (C7)	99.81	—	—	30	2.7794	0.1000

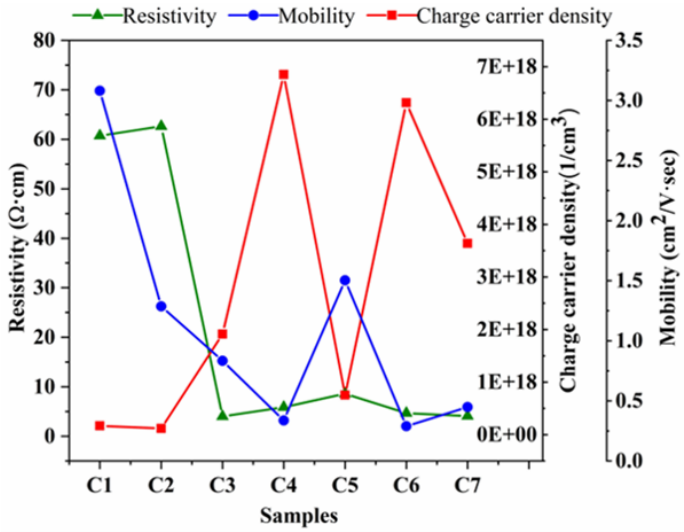

Figure 6. Results Obtained for Resistivity (Ω·cm), Charge Carrier Concentration (1/cm^3), and Mobility (cm^2/V·s) Plotted as a Function of The Relative Concentration of HMTA in The Precursor Solution

ture, as samples C1, C2, and C5 show spacings between rods, where material deposition is insufficient, which was expected to affect the mobility of the carriers, and was not the case. On the other hand, the surface of the ZnO rods in these same samples, appears to be relatively smooth, which could represent fewer defects and consequently a lower quantity of charge carriers. Contrastingly, samples C4, C6, and C7, are practically free of gaps and are composed by sub-micrometric structures with a nanostructured surface resulting in higher values for charge carriers.

3.4 Optical Properties

Figure 7 shows the photoluminescent emission spectra of all samples when excited them with a λ_{ex}= 325 nm, as well as excitation spectra for sample C7 when considering the emission λ_{em}= 395, 420 and 620 nm. Photoluminescence emission spectra for all samples (Figure 7b) presents the characteristic emission spectra for ZnO (Angulo-Rocha et al., 2017; Félix-Quintero et al., 2017; Ramos-Brito et al., 2011). It shows a narrow emission band centered around near-UV wavelength, which is associated to an exciton-related electronic transition. In addition, it exhibits a broad emission band in the visible range of the electromagnetic spectrum, typically associated with defects in the crystalline structure of ZnO. Additionally, besides the se two particular bands, an emission band can be found around 410-490 nm, which intensity will vary depending on the sample. Figure 8 presents a deconvolution of the emission spectra for sample C3, it can be observed that the spectrum itself can be seen as one composed of distinct emission bands centered around 387, 395, 411, 439, 602, and 688 nm. Referring to the works previous (Angulo-Rocha et al., 2017; Félix-Quintero et al., 2017; Ramos-Brito et al., 2011), emission bands were associated with electronic transitions between different states of energy introduced into the ZnO energy band gap due to its following intrinsic defects: neutral interstitial zinc (Zn_{i0}), zinc vacancies (V_{Zn}), interstitial zinc (Zn_i), oxygen antisite (O_{Zn}), and Interstitial oxygen (O_i). This according to the energy diagram in Figure 9. In this it is observed that the emission centered at 387 nm is associated with the electronic transition $Zn_{i0} \rightarrow$ VB, emission centered at 395 nm with the CB $\rightarrow V_{Zn}$ transition, emission centered at 411 nm at $Zn_{i0} \rightarrow V_{Zn}$ electronic transition, the emission of 439 nm to the electronic transition $Zn_i \rightarrow$ BV. The band centered at 602 nm at the CB $\rightarrow O_{zn}$ and CB $\rightarrow O_i$ transitions and finally, the band focused on 688 nm was associated with the electronic transitions $Zn_i \rightarrow Ozn$ and $Zn_i \rightarrow O_i$, which is consistent with what was reported Özgür et al. (2005b) and recently by Siva et al. (2019). These latter observed a yellow band (574-587) nm that they associate with the presence of Oi and a band between (678-729) nm associated with excess oxygen or oxygen vacancies (V_0) sites. Surely at the time of deconvolution of the emission spectrum (Figure 8) it was also possible have considered the occurrence of V_0, as reported in previous work for deposited ZnO using Spray Pyrolysis (Angulo-Rocha et al., 2017) where the presence was considered of V_0 due to the rel-

atively intense emission in the region of (460-510) nm, but as already it had been observed in previous work (Félix-Quintero et al., 2017; Ramos-Brito et al., 2011) and now in this one, apparently when the synthesis is by chemical bath deposition the emission in this region is relatively poor, which is why it was not considered. Low intensity Luminescent in the region of (460-510) is associated with the poor presence of V_0 because the synthesis is carried out in a oxygen-rich environment (Özgür et al., 2005b).

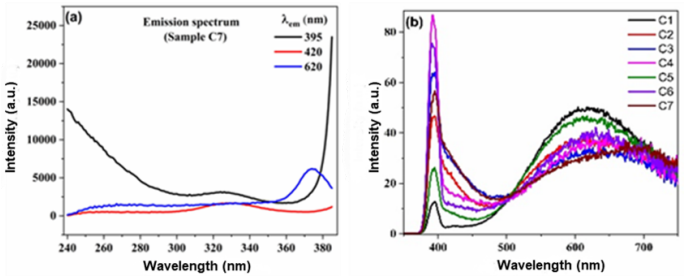

Figure 7. a) Excitation Spectra for Sample C7 when Considering The 395, 420 and 620 nm Emission Wavelengths as Well as b) Photoluminescent Emission Spectra of All Samples when Excited Them with a Wavelength of 325 nm

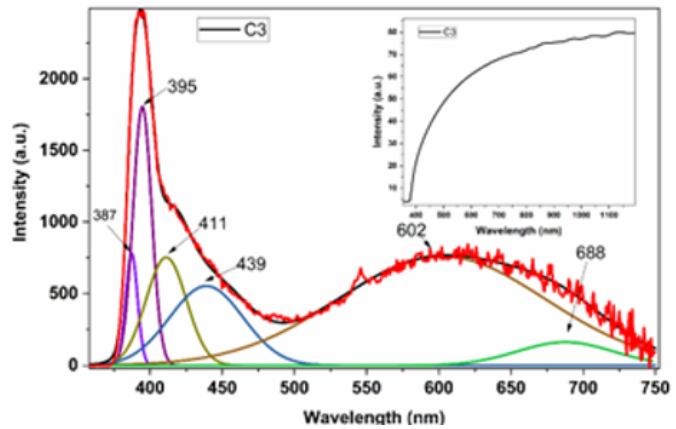

Figure 8. Deconvolution of The Emission Spectrum of Sample C3. It Shows Bands of Emission Centered at 387, 395, 411, 439, 602 and 688 nm that were Associated with The Presence of Defects in The Crystalline Structure of ZnO. The Insert Shows The Transmittance Spectrum for Sample C3 which is Representative of All Samples

Due to the position of the donor and acceptor defects in the "band gap" (see Figure 9) it can be concluded that the ones that mostly affect the conductivity of ZnO are: Zn_{i0}, Zn_i, and V_{Zn}, since the energy distances of O_{Zn} and O_i from VB are large enough involving high activation energy; considering this fact and in order to investigate a possible correlation, at least qualitative, between the quantities of these defects and the concentration of charge carriers measured by Hall effect, the

Table 4. Relative Percentage Amounts of The Donor Defects Zn_{i0}, Zn_i, and Acceptors V_{Zn} Calculated from The Intensities of Their Corresponding Photoluminescent Emission Bands

Sample	Amount of donor defects "n" (%)	Amount of acceptor defects "p" (%)	Difference "n"-"p" (%)
C1	0.701092351	2.546962517	-1.845870166
C2	12.32504424	8.688540241	3.636504000
C3	17.58026106	11.78783564	5.792425420
C4	20.05841157	9.975875551	10.08253602
C5	1.340338616	5.404254271	-4.063915654
C6	14.90788871	10.93850050	3.969388210
C7	21.13800263	12.48812969	8.649872935

percentage intensities of the emission bands centered at 387, 395, and 439 nm were calculated, and as a first approximation associated with the relative percentage amounts of the donor defects Zn_{i0}, Zn_i and acceptor V_{Zn}. Table 4 presents these results, it can be seen that samples C4, C7, C3, and C6 are the highest value, in order from highest to lowest, for the difference between the number of defects Zn_{i0}, Zn_i donors and V_{Zn} acceptor, consistent with those with the highest number of C4, C6, C7, and C3 charge carriers, almost in the same order from highest to lowest, except for the C6 shows that in principle the difference between defects should have been greater than C7 and C3 and less than C4. This seems to indicate that a correlation exists between the relative concentration of type "n" and "p" charge carriers and the difference of intensities for emission peaks associated with the bands for $Zn_{i0} \rightarrow$ VB, CB $\rightarrow V_{Zn}$ and $Zn_i \rightarrow$ BV. These results encourage the use of high resolution photoluminescence spectroscopy to deconvolute said emission bands to obtain enough precision to quantitatively measure the difference in intensities and therefore the difference between type "n" and "p" charge carriers in ZnO. This could place photoluminescence spectroscopy as an optical method for characterizations that until this day are done only via electrical techniques.

The insert of Figure 8 shows the transmittance spectrum for sample C3 which is representative of all samples. The transmittance for all samples was not greater than 70% in the visible region, being C1 the one with the lowest transmittance 40%. They all started with their value highest at 750 nm, in the case of C3 it starts at ~ 70% for 750 nm, and they presented a drop pronounced due to intrinsic defects in its crystalline structure. The energy band gap of all the samples were obtained using the Tauc method (Viezbicke et al., 2015), resulting in: 3.19, 2.8, 3.18, 3.25, 3.05, 3.26, and 3.19 eV for, C1, C2, ..., C7, respectively.

3.5 Implications of Morphology, Texture, and Crystallite Size on Electrical Properties

Figure 10 shows the resistivity as a function of: percentage of substrate-covered area, average diameter of the bars or thick-

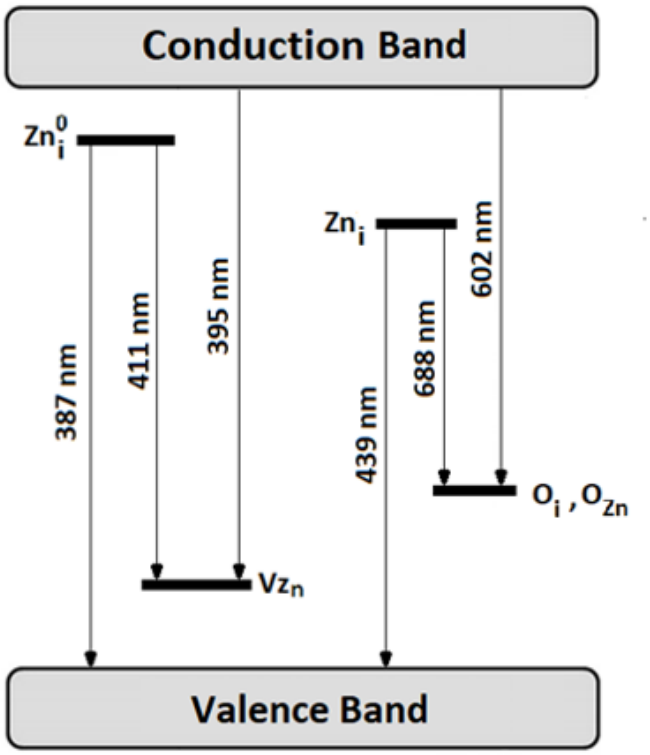

Figure 9. Energy Diagram that Shows Indistinctly The Different De-Excitation Paths for Bars or Sheets of ZnO

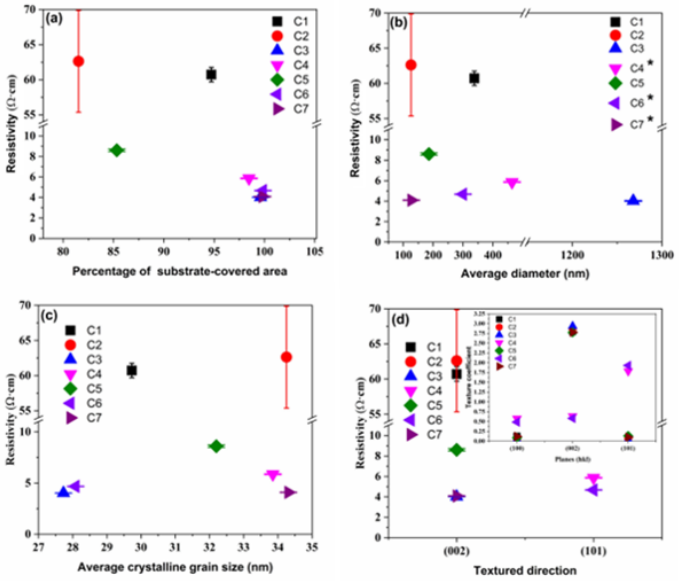

Figure 10. It Shows The Resistivity of All Samples as a Function of: a) Percentage of Substrate-Covered Area, b) Average Diameter of The Bars or Thickness of The Sheets, c) Average Crystalline Grain Size and d) Texture Direction

ness of the sheets, average crystalline grain size and texture direction, of samples. Figure 10a shows that for all samples there is the tendency that the highest the percentage of substrate-covered area, the smaller the resistivity except for C1. This exception can be attributed to the fact that it is C1 the one having the least percentage of donor defects (see Table 4). Figures 10a and 10b show for samples C1, C2, C3, and C5 that the greatest the diameter of the bars, the greater the percentage of substrate-covered area, therefore, the contribution that diameter of the bars has in the resistivity is implicitly contemplated when considering the contribution that substrate-covered area has in the resistivity.

A correlation between resistivity and texture coefficient was not found. Samples C1, C2, C3, C5, and C7, textured in the <001> direction have too similar texture coefficients, with a relative percentage difference between them less than 5% (see Table 4), while the resistivity between them differs from up to an order of magnitude (see Figure 6).

The mobility of the charge carriers in a thin film is necessarily influenced by the crystalline grain size, percentage of substrate-covered area, texturing direction, and microstructure of the sample in question. Figure 6 and Table 3 show that mobility for samples C1, C2, C3, C5, and C7, textured in the direction <001>, increases as the substrate-covered area increases even if the crystalline grain size decreases, being then the substrate-covered area a preponderant factor in mobility. This happens even when a decrease in the crystalline grain size could implies an increase of the crystal dislocations that should means greater dispersion centers for charge carriers and therefore less mobility of them.

The results shown in Figure 6, Table 1 and Table 1 show that when you have a covered percentage of the area larger than 95% the major factor in mobility appears to be the crystalline grain size, just as if the amount of crystal dislocations dominates mobility. This was observed when mobility comes from 3.0803 $cm^2/V{\cdot}s$ for sample C1 that has a substrate-covered area of 94.72% and particle size of 29,731 nm to mobility of 0.8334 $cm^2/V{\cdot}s$ for the C3 sample that has a substrate-covered area of 99.61% and grain size of 27.731 nm.

The change in the microstructure of the thin film could be a relevant factor in mobility. This was observed when mobility of sample C7 that has substrate-covered area of 99.81% was less in an up to a 65.2% than mobility of C2 that has substrate-covered area of 81.52%.

In dealing with the samples C4 and C6 textured in the direction <101> their values for the crystalline grain size, percentage of substrate-covered area, texturing direction and microstructure are too similar, which is consistent with the similarity between its values for resistivity, charge carrier concentration and mobility. The small difference between their values for the charge carrier concentration is consistent with the difference between their values for the relative percentage amounts of donor and acceptor defects (see Table 4).

4. CONCLUSIONS

The deposit by spin coating followed by chemical bath allowed the synthesis of ZnO films. The seven samples resulted in microstructured films. The C1, C2, C3, C4, and C5 films were made up entirely of ZnO bars that were moderately oriented perpendicular to the substrate and with apparently hexagonal cross section, while films C6 and C7 were made up of corn flake-like structures oriented almost perpendicular to the substrate plane. All ZnO bars show a nodular type growth and nanostructured hexagonal cross section with an average roughness of the order of crystallite grain size.

The experiment allowed the synthesis of ZnO films with hexagonal crystalline structure (a= 3,250 Å and c= 5,195 Å), average crystalline grain size of 31.95 nm and a shaped surface, for the most of the samples, by hexagonal bars with diameters that varies between 126 and 1268 nm. The increase in the diameter of the bars induces a higher substrate-covered area.

The synthesis process favors two texture directions, (002) and (101) without noticeable changes between the texture coefficients for both. The <101> textured ZnO films resulted with the highest number of charge carrier values of around 6.5×10^{18} $1/cm^3$, but with the lowest mobility with values of around the 0.32 $cm^2/V{\cdot}s$. The higher the percentage of substrate-covered area of ZnO films, the lower their resistivity, regardless of their morphology and texture. The <001> texturized sample C3 resulted with the lowest resistivity of 4.02 Ω·cm. The mobility in ZnO films resulted mainly influenced by substrate-covered area, this when its value is less than 95%, while for higher values the mobility is dominated by the crystalline grain size.

A new optical parameter resulted from the difference between photoluminescent emissions associated with donor defects (Zn_{i0} y Zn_i) and V_{Zn} acceptors that could be considered as an indicator of the charge carrier concentration. The greater the difference, the greatest the concentration of n-type charge carriers. These results encourage the use of high resolution photoluminescence spectroscopy to quantitatively measure the difference between type "n" and "p" charge carriers in ZnO. This could place photoluminescence spectroscopy as an optical method for characterizations that until this day are done only via electrical techniques.

5. ACKNOWLEDGMENT

Authors wish to express their gratitude to the National Council of Science and Technology (CONACYT) for the master scholarships granted to: C. López-Esmerio and C. Ruiz-Rojas. They would also like to acknowledge the technical support of: Dr. F. J. S. Rodriguez in synthesis process, Dr. Omar Novelo in SEM characterization and Dr. Rogelio Fragoso in AFM analysis.

REFERENCES

Angulo-Rocha, J., O. Velarde Escobar, C. Yee Rendón, G. Atondo Rubio, R. Millan-Almaraz, E. Camarillo-García, M. García-Hipólito, and F. Ramos-Brito (2017). Morphological, Structural and Optical Properties of ZnO Thin Solid Films Formed by Nanoleafs or Micron/Submicron Cauliflowers. *Journal of Luminescence*, **185**; 306–315

Bian, J., X. Li, C. Zhang, L. Chen, and Q. Yao (2004). Synthesis and Characterization of Two-Layer-Structured ZnO pn Homojunctions by Ultrasonic Spray Pyrolysis. *Applied Physics Letters*, **84**(19); 3783–3785

Bindu, P. and S. Thomas (2014). Estimation of Lattice Strain in ZnO Nanoparticles: X-Ray Peak Profile Analysis. *Journal of Theoretical and Applied Physics*, **8**(4); 123–134

Carcia, P., R. McLean, and M. Reilly (2006). High-Performance ZnO Thin-Film Transistors on Gate Dielectrics Grown by Atomic Layer Deposition. *Applied Physics Letters*, **88**(12); 123509

Chandrasekaran, M. and M. Pandurangan (2016). In Vitro Selective Anti-Proliferative Effect of Zinc Oxide Nanoparticles Against Co-Cultured C2C12 Myoblastoma Cancer and 3T3-L1 Normal Cells. *Biological Trace Element Research*, **172**(1); 148–154

Chang, S. B., H. U. Chae, and H. S. Kim (2017). Structural, Optical, Electrical and Morphological Properties of Different Concentration Sol-Gel ZnO Seeds and Consanguineous ZnO Nanostructured Growth Dependence on Seeds. *Journal of Alloys and Compounds*, **729**; 571–582

Chen, T. L. and J. M. Ting (2016). Correlation Between Seed Layer Characteristics and Structures/Properties of Chemical Bath Synthesized ZnO Nanowires. *Surface and Coatings Technology*, **303**; 197–202

Chou, S. M., L. G. Teoh, W. H. Lai, Y. H. Su, and M. H. Hon (2006). ZnO: Al Thin Film Gas Sensor for Detection of Ethanol Vapor. *Sensors*, **6**(10); 1420–1427

Cullity, B. and S. Stock (2001). *Elements of X-Ray Diffraction Third Edition*. Prenrice Hall, New Jersey

Félix-Quintero, H., J. Angulo-Rocha, S. Murrieta, A. Hernández, G. Camarillo, J. Flores, C. Alejo-Armenta, M. García-Hipolito, and F. Ramos-Brito (2017). Study on Grow Process and Optical Properties of ZnO Microrods Synthesized by Hydrothermal Method. *Journal of Luminescence*, **182**; 107–113

Gayral, B. (2017). LEDs for Lighting: Basic Physics and Prospects for Energy Savings. *Comptes Rendus Physique*, **18**(7-8); 453–461

Gonçalves, G., V. Grasso, P. Barquinha, L. Pereira, E. Elamurugu, M. Brignone, R. Martins, V. Lambertini, and E. Fortunato (2011). Role of Room Temperature Sputtered High Conductive and High Transparent Indium Zinc Oxide Film Contacts on The Performance of Orange, Green, and Blue Organic Light Emitting Diodes. *Plasma Processes and Polymers*, **8**(4); 340–345

Gupta, J., P. Bhargava, and D. Bahadur (2015). Fluorescent ZnO for Imaging and Induction of DNA Fragmentation and ROS-Mediated Apoptosis in Cancer Cells. *Journal of Materials Chemistry B*, **3**(9); 1968–1978

Hanley, C., J. Layne, A. Punnoose, K. Reddy, I. Coombs,

A. Coombs, K. Feris, and D. Wingett (2008). Preferential Killing of Cancer Cells and Activated Human T Cells Using ZnO Nanoparticles. *Nanotechnology*, **19**(29); 295103

Hassan, H. F. H., A. M. Mansour, A. M. H. Abo-Youssef, B. E. Elsadek, and B. A. S. Messiha (2017). Zinc Oxide Nanoparticles as a Novel Anticancer Approach; In Vitro and In Vivo Evidence. *Clinical and Experimental Pharmacology and Physiology*, **44**(2); 235–243

Kalita, A. and M. Kalita (2015). Size Dependence of Lattice Parameters in ZnO Nanocrystals. *Applied Physics A*, **121**(2); 521–524

Karthikeyan, C., P. Arunachalam, K. Ramachandran, A. M. Al-Mayouf, and S. Karuppuchamy (2020). Recent Advances in Semiconductor Metal Oxides with Enhanced Methods for Solar Photocatalytic Applications. *Journal of Alloys and Compounds*, **828**; 154281

Kc, B., S. N. Paudel, S. Rayamajhi, D. Karna, S. Adhikari, B. G. Shrestha, and G. Bisht (2016). Enhanced Preferential Cytotoxicity Through Surface Modification: Synthesis, Characterization and Comparative In Vitro Evaluation of TritonX-100 Modified and Unmodified Zinc Oxide Nanoparticles in Human Breast Cancer Cell (MDA-MB-231). *Chemistry Central Journal*, **10**(1); 2–10

Kim, K. K., J. H. Song, H. J. Jung, W. K. Choi, S. J. Park, and J. H. Song (2000). The Grain Size Effects on The Photoluminescence of ZnO/α-Al_2O_3 Grown by Radio-Frequency Magnetron Sputtering. *Journal of Applied Physics*, **87**(7); 3573–3575

Lu, J., S. Fujita, T. Kawaharamura, and H. Nishinaka (2007). Roles of Hydrogen and Nitrogen in p-Type Doping of ZnO. *Chemical Physics Letters*, **441**(1-3); 68–71

Lu, Y., H. Ni, Z. Mai, and Z. Ren (2000). The Effects of Thermal Annealing on ZnO Thin Films Grown by Pulsed Laser Deposition. *Journal of Applied Physics*, **88**(1); 498–502

Muiva, C., T. Sathiaraj, and K. Maabong (2011). Effect of Doping Concentration on The Properties of Aluminium Doped Zinc Oxide Thin Films Prepared by Spray Pyrolysis for Transparent Electrode Applications. *Ceramics International*, **37**(2); 555–560

Nanda, S. S., M. J. Kim, K. Kim, G. C. Papaefthymiou, S. T. Selvan, and D. K. Yi (2017). Recent Advances in Biocompatible Semiconductor Nanocrystals for Immunobiological Applications. *Colloids and Surfaces B: Biointerfaces*, **159**; 644–654

Nguyen, T. M. T., P. W. Wang, H. M. Hsu, F. Y. Cheng, D. B. Shieh, T. Y. Wong, and H. J. Chang (2019). Dental Cement's Biological and Mechanical Properties Improved by ZnO Nanospheres. *Materials Science and Engineering: C*, **97**; 116–123

Özgür, Ü., Y. I. Alivov, C. Liu, A. Teke, M. Reshchikov, S. Doğan, V. Avrutin, S. J. Cho, Morkoç, and H (2005a). A Comprehensive Review of ZnO Materials and Devices. *Journal of Applied Physics*, **98**(4); 11

Özgür, Ü., Y. I. Alivov, C. Liu, A. Teke, M. Reshchikov, S. Doğan, V. Avrutin, S. J. Cho, Morkoç, and H (2005b). A Comprehensive Review of ZnO Materials and Devices. *Journal of Applied Physics*, **98**(4); 11

Pandurangan, M., G. Enkhtaivan, and D. H. Kim (2016). Anticancer Studies of Synthesized ZnO Nanoparticles Against Human Cervical Carcinoma Cells. *Journal of Photochemistry and Photobiology B: Biology*, **158**; 206–211

Park, S. H., J. B. Park, and P. K. Song (2010). Characteristics of Al-Doped, Ga-Doped and In-Doped Zinc-Oxide Films as Transparent Conducting Electrodes in Organic Light-Emitting Diodes. *Current Applied Physics*, **10**(3); S488–S490

Rahman, F. (2019). Zinc Oxide Light-Emitting Diodes: a Review. *Optical Engineering*, **58**(1); 010901

Ramos-Brito, F., C. Alejo-Armenta, M. García-Hipólito, E. Camarillo, and C. Falcony (2011). Synthesis of Zinc Oxide Microrods and Nano-Fibers with Dominant Exciton Emission at Room Temperature. *Journal of Luminescence*, **131**(5); 874–879

Rana, A. U. H. S., J. Y. Lee, A. Shahid, and H. S. Kim (2017). Growth Method-Dependent and Defect Density-Oriented Structural, Optical, Conductive, and Physical Properties of Solution-Grown ZnO Nanostructures. *Nanomaterials*, **7**(9); 266

Rasband, W. (2012). ImageJ: Image Processing and Analysis in Java. *Astrophysics Source Code Library*; ascl–1206

Shinde, V. R., T. P. Gujar, T. Noda, D. Fujita, A. Vinu, M. Grandcolas, and J. Ye (2010). Growth of Shape-and Size-Selective Zinc Oxide Nanorods by a Microwave-Assisted Chemical Bath Deposition Method: Effect on Photocatalysis Properties. *Chemistry–A European Journal*, **16**(34); 10569–10575

Siva, V., K. Park, M. S. Kim, Y. J. Kim, G. J. Lee, M. J. Kim, and Y. M. Song (2019). Mapping The Structural, Electrical, and Optical Properties of Hydrothermally Grown Phosphorus-Doped ZnO Nanorods for Optoelectronic Device Applications. *Nanoscale Research Letters*, **14**(1); 1–9

Solati, E. and D. Dorranian (2017). Estimation of Lattice Strain in ZnO Nanoparticles Produced by Laser Ablation at Different Temperatures. *Journal of Applied Spectroscopy*, **84**(3); 490–497

Suhaimi, L. and A. Yuwono (2019). Optical Properties of ZnO Nanorods Derived from Chemical Bath Deposition Process with Different Seeds Solution Concentration. In *IOP Conference Series: Materials Science and Engineering*, **541**; 012034

Vandebriel, R. J. and W. H. De Jong (2012). A Review of Mammalian Toxicity of ZnO Nanoparticles. *Nanotechnology, Science and Applications*, **5**; 61

Viezbicke, B. D., S. Patel, B. E. Davis, and D. P. Birnie III (2015). Evaluation of The Tauc Method for Optical Absorption Edge Determination: ZnO Thin Films as a Model System. *Physica Status Solidi (B)*, **252**(8); 1700–1710

Wahab, R., N. Kaushik, F. Khan, N. K. Kaushik, E. H. Choi, J. Musarrat, and A. A. Al-Khedhairy (2016). Self-Styled ZnO Nanostructures Promotes The Cancer Cell Damage and Supresses The Epithelial Phenotype of Glioblastoma.

Scientific Reports, **6**(1); 1–13

Wang, Y., W. Tang, and L. Zhang (2015). Crystalline Size Effects on Texture Coefficient, Electrical and Optical Properties of Sputter-Deposited Ga-Doped ZnO Thin Films. *Journal of Materials Science & Technology*, **31**(2); 175–181

Weisbuch, C. (2018). Historical Perspective on The Physics of Artificial Lighting. *Comptes Rendus Physique*, **19**(3); 89–112

Wu, W. Y., T. L. Chen, and J. M. Ting (2010). Effects of Seed Layer Precursor Type on The Synthesis of ZnO Nanowires Using Chemical Bath Deposition. *Journal of The Electrochemical Society*, **157**(8); K177

Yamada, T., A. Miyake, S. Kishimoto, H. Makino, N. Yamamoto, and T. Yamamoto (2007). Low Resistivity Ga-Doped ZnO Thin Films of Less Than 100 nm Thickness Prepared by Ion Plating with Direct Current Arc Discharge. *Applied Physics Letters*, **91**(5); 051915

Yeap, G. (2013). Smart Mobile SoCs Driving The Semiconductor Industry: Technology Trend, Challenges and Opportunities. In *IEEE International Electron Devices Meeting*. IEEE; 1–3

Zhang, D., J. Zhang, Y. Cheng, L. Yuan, and X. Miao (2010). Ultraviolet Emission and Electrical Properties of Aluminum-Doped Zinc Oxide Thin Films with Preferential C-Axis Orientation. *Journal of The American Ceramic Society*, **93**(10); 3291–3298

Zhang, Z., É. Ódor, D. Farkas, B. Jóni, G. Ribárik, G. Tichy, S. H. Nandam, J. Ivanisenko, M. Preuss, and T. Ungár (2020). Dislocations in Grain Boundary Regions: The Origin of Heterogeneous Microstrains in Nanocrystalline Materials. *Metallurgical and Materials Transactions A*, **51**(1); 513–530

Zhu, D. and Q. Zhou (2019). Action and Mechanism of Semiconductor Photocatalysis on Degradation of Organic Pollutants in Water Treatment: a Review. *Environmental Nanotechnology, Monitoring & Management*, **12**; 100255

ZKTang, G., P. Y. Wong, M. Kawasaki, A. Ohtomo, H. Koinuma, and Y. Segawa (1998). Room-Temperature Ultraviolet Laser Emission from Self-Assembled ZnO Microcrystalline Thin Films. *Applied Physics Letters*, **72**; 3270–3272

